Invited feature article

Investigation of photophysicochemical properties of zinc phthalocyanines conjugated to metallic nanoparticles

Edith Dube, Njemuwa Nwaji, David O. Oluwole, John Mack, Tebello Nyokong*

Department of Chemistry, Rhodes University, Grahamstown 6140, South Africa

A B S T R A C T

The syntheses of zinc(II) tetra–[3–(4–phenoxy) (propanoic acid) phthalocyanine] (**2**) and zinc(II) mono–[3–(4–phenoxy) (propanoic acid) phthalocyanine (**3**) are reported in this work. Compounds **2** and **3** were covalently linked to glutathione capped silver (AgNPs–GSH), gold (AuNPs–GSH) and silver-gold alloy (Ag$_3$Au$_1$NPs–GSH) nanoparticles (NPs) via an amide bond formation to afford the conjugates: **2**–AgNPs–GSH, **3**–AgNPs–GSH, **2**–AuNPs–GSH, **3**–AuNPs–GSH, **2**–Ag$_3$Au$_1$NPs–GSH and **3**–Ag$_3$Au$_1$NPs–GSH. The photophysicochemical behaviours of the compounds and their conjugates with NPs were assessed in solution. The conjugates afforded a decrease in fluorescence quantum yields and lifetimes with improved triplet quantum yields in comparison to the compounds. Accordingly, the AgNPs and AuNPs conjugates with the compounds afforded high singlet quantum yields. On the contrary, the conjugates of the alloy afforded decreased singlet quantum yields probably due to the screening effect. The compounds and their conjugates with NPs could serve as a viable and efficacious photosensitizer for photodynamic therapy.

© 2017 Elsevier B.V. All rights reserved.

1. Introduction

Phthalocyanines (Pcs) are continuously receiving pivotal attention from researchers due to their unique physicochemical properties [1]. Traditionally, Pcs have been exploited as dyes and pigments [2] in various industries such as textile and automobile to mention a few. Pcs can be functionalized to allow for a variety of applications [3–5] including in nonlinear optics [6–10], photodynamic therapy (PDT) [11,12] and photovoltaics [13]. Of particular interest is their ability to generate singlet oxygen which is the primary agent for cancer cell death in PDT [11,12].

The presence of heavy atoms, either as part or external to the Pcs, enhances excitation to a triplet state through spin orbit coupling (SOC). High SOC values enhance the kinetics of both radiative and non-radiative transitions between states with different spin. Intersystem crossing (ISC) is thus observed mostly in systems containing high atomic number elements, a phenomenon, known as heavy atom effect [14]. The central metal in metallophthalocyanines (MPcs) and the conjugated nanoparticles (NPs) have been reported to enhance the triplet and singlet oxygen quantum yields of the phthalocyanines due to the heavy atom

effect which encourages intersystem crossing to the triplet state [15] as explained above. Enhanced triplet state quantum yields leads to improved singlet oxygen generation, since the latter is generated when the triplet state of Pc interacts with the ground state molecular oxygen.

In this work, two novel zinc phthalocyanines were synthesised and covalently linked to glutathione (GSH) functionalised gold (AuNPs), silver (AgNPs) and silver-gold alloy (Ag$_3$Au$_1$NPs) nanoparticles (whose syntheses has been reported before [16–19]). Symmetrical and asymmetrical phthalocyanines have been linked to AuNPs [19–23] or AgNPs [24] with improved triplet state and singlet oxygen quantum yields as well as improved PDT activity. Symmetrical Pcs have been linked to AgAuNPs for photophysical and nonlinear optical studies [16,25]. This work reports on the conjugates of AuNPs, AgNPs and Ag$_3$Au$_1$NPs (numbers in brackets are the ratios of Ag and Au) with symmetrical and asymmetrical phthalocyanines containing the same substituents for the first time. The phthalocyanines employed in this work are: zinc(II) tetra–[3–(4–phenoxy) (propanoic acid)phthalocyanine] (**2**) and zinc(II) mono–[3–(4–phenoxy) (propanoic acid) phthalocyanine] (**3**). The choice of propanoic acid as a substituent is based on the

---

* Corresponding author.
  E-mail address: t.nyokong@ru.ac.za (T. Nyokong).

fact that porphyrins containing propanoic acid (such as the Uroporphyrins) have been employed successfully for PDT [11].

Glutathione was employed for the functionalization of the NPs due to availability of sulfhydryl (SH), and amino acid (–NH$_2$) in its molecular structure. The SH was coordinated to the surface of the NPs via sulfur to metal interaction and the NH$_2$ was covalently linked to the activated —COOH terminal end of the Pcs via amide bond formation to afford the conjugates. The MPcs, NPs and the conjugates were characterized and the photophysicochemical properties were studied.

2. Experimental

2.1. Materials

Ultra-pure water was obtained from a Milli–Q Water System (Millipore Corp, Bedford, MA, USA), 3-(4-hydroxyphenyl)-propionic acid, potassium carbonate, 1-pentanol, zinc (II) acetate dihydrate, 1,8-diazobicylo[5.4.0]undec-7-ene (DBU), zinc phthalocyanine (ZnPc), KOH, chloroform, N,N'-dicyclohexylcarbodiimide (DCC), 4-(dimethylamino)pyridine (DMAP), 1,3-diphenylisobenzofuran (DPBF), dicyanobenzene and anthracene-9,10-bis-methylmalonate (ADMA) were purchased from Sigma–Aldrich. Tetrahydrofuran (THF), N,N-dimethyl formamide (DMF) and dimethyl sulphoxide (DMSO) were purchased from Merck. All other reagents and solvents were obtained from commercial suppliers and used as received. Silica gel 60 (0.063–0.200 mm) for column chromatography was used for the purification processes. AlPcSmix [26] (containing a mixture of sulfonated derivatives and used as a standard for singlet oxygen quantum yields in water) and 4-nitrophthalonitrile [27] were synthesized as reported in the literature. Glutathione (GSH) capped AgNPs (AgNPs-GSH [18]), AuNPs (AuNPs-GSH [19]), and Ag$_3$Au$_1$NPs (Ag$_3$Au$_1$NPs-GSH [16]) nanoparticles were synthesized as reported in literature. Numbers in brackets are the ratios of Ag and Au for the latter.

2.2. Equipment

Infrared spectra were acquired on a Bruker ALPHA FT–IR spectrometer with universal attenuated total reflectance (ATR) sampling accessory. ^{1}H NMR spectra were recorded on a Bruker AVANCE II 600 MHz NMR spectrometer using tetramethylsilane (TMS) as an internal reference. Elemental analyses were performed using a Vario-Elementar Microcube ELIII. Mass spectra data were collected on a Bruker AutoFLEX III Smart-beam TOF/TOF mass spectrometer using α-cyano-4-hydrocinnamic acid as the matrix. X-ray powder diffraction patterns were recorded using a Cu K radiation (1.5405°A, nickel filter), on a Bruker D8 Discover equipped with a proportional counter and the data was processed using the Eva (evaluation curve fitting) software. The morphologies of the NPs and their conjugates were assessed using a transmission electron microscope (TEM), ZEISS LIBRA model 120 operated at 90 kV and iTEM software was used for TEM micrographs processing. Elemental compositions of the NPs and the conjugates were qualitatively determined using an energy dispersive X-ray spectroscopy (EDX), INCA PENTA FET coupled to the VAGA TESCAM operated at 20 kV accelerating voltage. Ground state electronic absorption was measured using a Shimadzu UV-2550 spectrophotometer. Fluorescence excitation and emission spectra were measured on a Varian Eclipse spectrofluorimeter using a 360–1100 nm filter. Excitation spectra were recorded using the Q–band of the emission spectra. Fluorescence lifetimes were measured using a time correlated single photon counting setup (TCSPC) (FluoTime 300, Picoquant GmbH) with a diode laser (LDH-P-670, Picoquant GmbH, 20 MHz repetition rate, 44 ps pulse width). Details have been provided before [23].
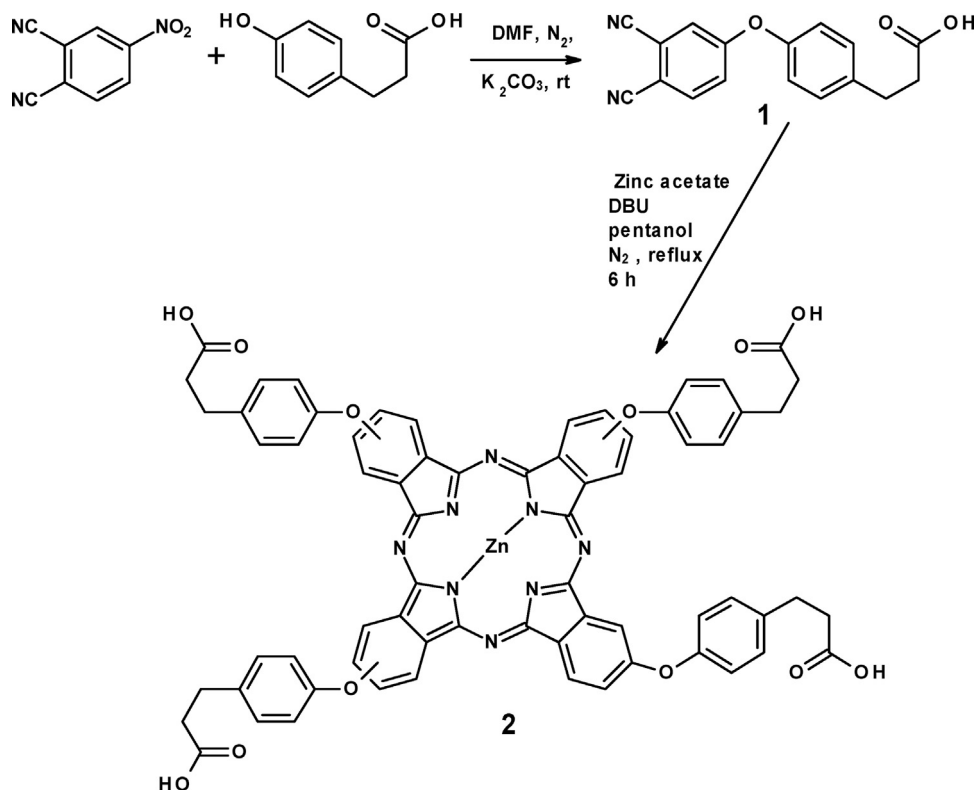
Scheme 1. Synthesis of zinc(II) tetra–[3-(4-phenoxy) propanoic acid) phthalocyanine] (complex **2**).
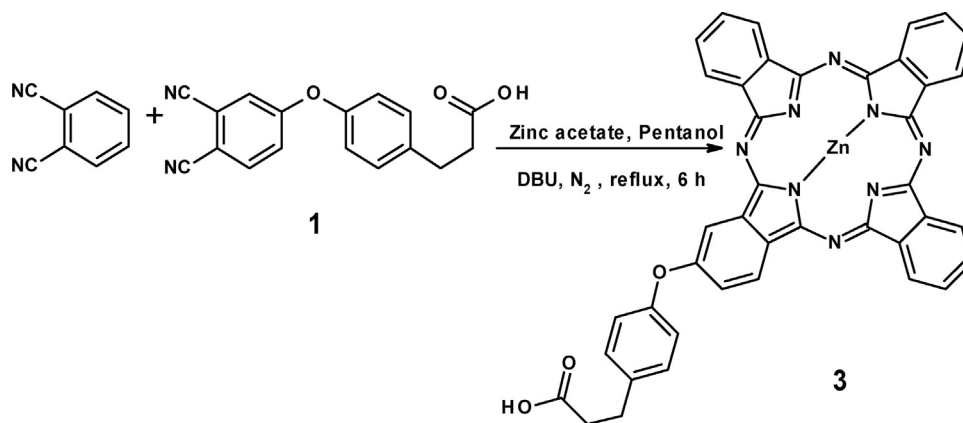
Scheme 2. Synthesis of low symmetry zinc (II) mono–(4-phenoxy) propanoic acid) phthalocyanine (complex **3**).

Triplet quantum yields were determined using a laser flash photolysis system. The excitation pulses were produced using a tunable laser system consisting of an Nd:YAG laser (355 nm, 135 mJ/4–6 ns) pumping an optical parametric oscillator (OPO, 30 mJ/3–5 ns) with a wavelength range of 420–2300 nm (NT-342B, Ekspla), as reported before [28].

Irradiation for singlet oxygen quantum yield was performed using a general electric quartz lamp (300 W) as described in the literature [24]. Light intensity was measured with a POWER MAX 5100 (Molelectron detector incorporated) power meter and was found to be 4.3×10^{15} photons $cm^{-2} s^{-1}$.

Magnetic circular dichroism (MCD) spectra were measured with a Chirascan plus spectrodichrometer equipped with a 1 T (tesla) permanent magnet by using both the parallel and antiparallel fields. The conventions of Piepho and Schatz are used to describe the sign of the MCD signal and the Faraday terms [29].

2.3. Theoretical calculations

The optimized structures of complexes **2** and **3** (Fig. S1, electronic Supplementary information, ESI) were obtained using the B3LYP functional of the Gaussian 09 software package with SDD basis sets [30]. TD-DFT calculations were carried out using the CAM-B3LYP functional with SDD basis sets. The CAM-B3LYP functional contains a long range connection that provides more accurate results for transitions with significant charge transfer character [31].

2.4. Syntheses

#### 2.4.1. 3(4-Phenoxy)-propanoic acid) phthalonitrile (**1**)

3-(4-Hydroxyphenyl)-propionic acid (1.44 g, 8.66 mmol) and 4-nitrophthalonitrile (1.5 g, 8.66 mmol) were dissolved in DMF (20 mL) under nitrogen atmosphere and the mixture was stirred at room temperature for 15 min. Finely ground K_2CO_3 (2.11 g,15.31 mmol) was added thereafter, and the reaction mixture was left to stir for a further 36 h at room temperature. The mixture was then added to ice water (150 mL). The resulting precipitate was filtered off, thoroughly washed with water, dried and recrystallized from ethanol to give complex **1**. Yield: 2.24 g (89%). IR [cm^{-1}]: 3300 (COOH) 2890–3030 (C—H), 2230 (C≡N), 1668-1583 (C=C), 1437-1387 (C—O), 1322-1275 (C—O), 1228 (Ar-O-Ar). ^{1}H NMR (DMSO–d_6): δ, ppm 7.89 (d, J = 7.52 Hz, 1H, Ar–H), 7.56 (d, J = 7.35 Hz, 1H, Ar–H), 7.37–7.32 (m, 3H, Ar–H), 7.12 (m, 2H, Ar–H), 3.48 (s, 1H, OH),
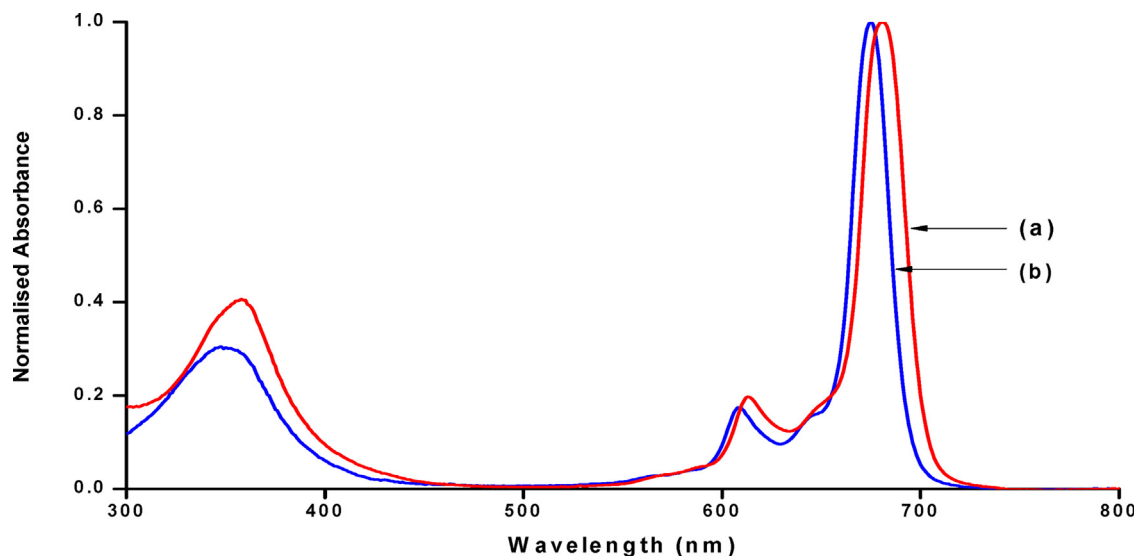

Fig. 1. Absorption spectra of complex **2** (a) and complex **3** (b), solvent = DMSO.

Table 1
Photophysicochemical parameters of complexes **2** and **3** and their conjugates with nanoparticles, solvent = DMSO.

Samples	Size (nm)[a]	λ_{abs} (nm)[b]	Pc loading (μg/mg)	Φ_F[c] (±0.01)	$\tau_{F(ns)}$ (±0.01)	τ_0 (ns)	Φ_T (±0.02)	τ_{isc} (ns)(±0.04)	τ_T (μs)	$\Phi_{\Delta(\pm0.01)}$[c]
Complex **2**	–	680	–	0.19 (<0.01)	3.36	17.68	0.54	6.22	264	0.47
2-AgNPs-GSH	14.7 (11.1)	680 (426)	9	0.11	2.95	26.82	0.67	4.40	271	0.54 (0.04)
2-AuNPs-GSH	14.9 (13.6)	679 (542)	27	0.03 (<0.01)	2.87	95.67	0.70	4.10	305	0.58 (0.15)
2-Ag₃Au₁NPs–GSH	17.3 (15.1)	678 (443)	41	0.04	2.87	71.75	0.69	4.16	314	0.39 (0.08)
Complex **3**	–	675	–	0.18 (<0.01)	3.21	17.83	0.73	4.39	233	0.55
3-AgNPs-GSH	12.2 (11.1)	674 (432)	10	0.16	3.10	19.38	0.82	3.78	274	0.69 (0.05)
3-AuNPs-GSH	13.8 (13.6)	674 (530)	20	0.02 (<0.01)	2.98	149.0	0.87	3.42	262	0.72 (0.23)
3-Ag₃Au₁NPs–GSH	16.5 (15.1)	673 (~440)	28	0.13	3.17	24.38	0.81	3.91	290	0.46 (0.11)

[a] Sizes in brackets are for NPs alone from XRD.

[b] Values in brackets are the SPR band of the NPs following conjugation. SPR bands of AgNPs and AuNPs alone are 405 nm and 532 nm, respectively. Silver in Ag₃Au₁NPs shows the peak at 408 nm and the AuNPs peak is not clear.

[c] Values in water in brackets.
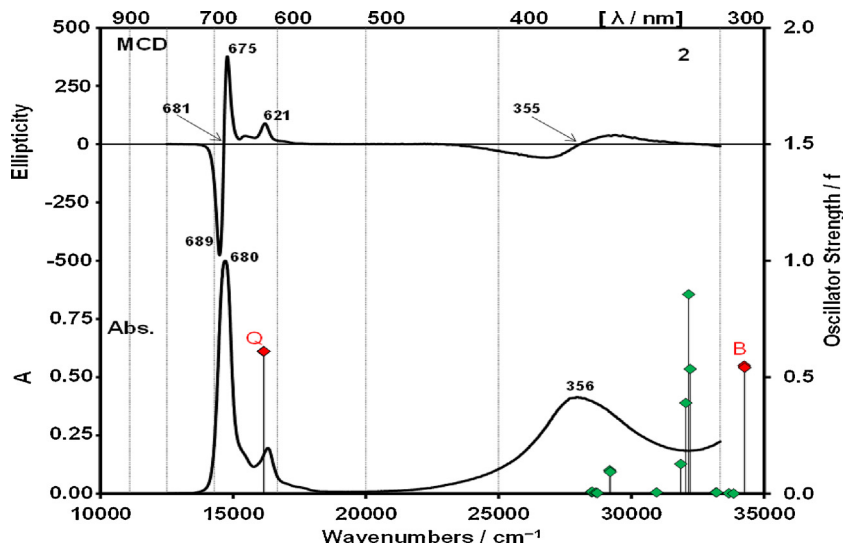
Fig. 2. Absorption and MCD spectra of complex **2** in DMSO. The calculated TD-DFT spectrum for the B3LYP optimized geometry is plotted against a secondary axis. Red diamonds are used to highlight bands associated with the Q and B bands of Gouterman's 4-orbital model. Details of the calculation are provided in Table S1. (For interpretation of the references to colour in this figure legend, the reader is referred to the web version of this article.)
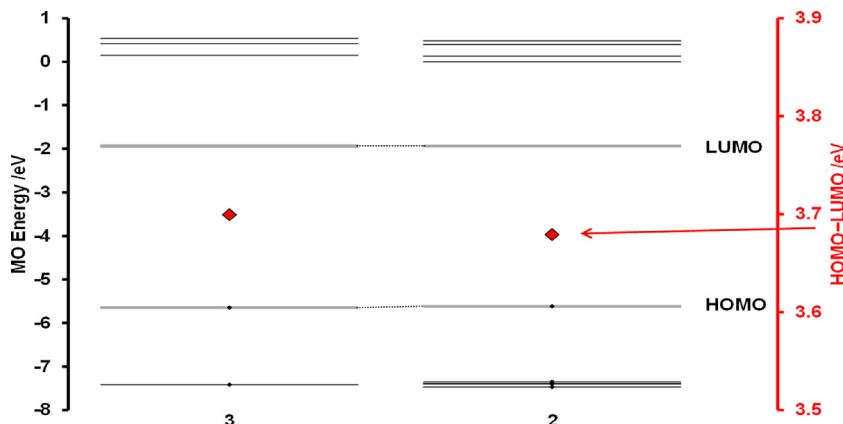
Fig. 3. The molecular orbital energies and HOMO–LUMO gaps of complex **2** and **3**. The HOMO–LUMO gaps are highlighted with red diamonds and are plotted against a secondary axis. Occupied MOs are denoted with small black diamonds and the frontier π-MOs are highlighted with gray lines. Dotted lines are used to highlight the relative destabilization of the HOMO of complex **2**. (For interpretation of the references to colour in this figure legend, the reader is referred to the web version of this article.)
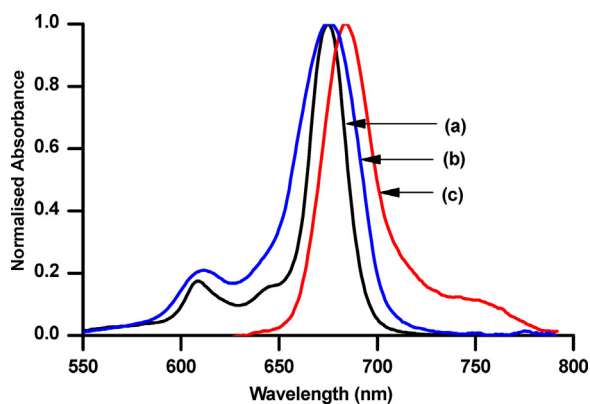
Fig. 4. Absorption (a), excitation (b) and emission (c) spectra of complex **3** (excitation = 607 nm, solvent = DMSO).

2.85 (t, J = 5.17 Hz, 2H, CH$_2$), 2.55 (t, J = 6.54 Hz, 2H, CH$_2$). Anal. Calc. for (C$_{17}$H$_{12}$N$_2$O$_3$): C, 69. 86; H, 4.14; N, 9.58. Found: C, 68.69: H, 3.89; N, 9.87.

2.4.2. Zinc(II) tetra–[3–(4–phenoxy) (propanoic acid) phthalocyanine] (**2**)

A mixture of 3-(4-(phenoxy)-propanoic acid phthalonitrile (**1**) (0.25 g, 0.86 mmol), dry 1–pentanol (3 mL), zinc(II) acetate dihydrate (0.25 g, 1.1 mmol) and DBU (0.3 mL) was transferred into a round bottom flask. The reaction mixture was refluxed at 180 °C for 6 h with constant stirring in the presence of nitrogen. After 6 h, the reaction mixture was cooled to room temperature, methanol was added and the mixture centrifuged several times with methanol. The product (complex **2**) was dried under vacuum and purified by column chromatography (silica gel, THF-methanol, 9:1). Yield: 0.46 g (43%). IR (cm^{-1}): 3420 (COOH), 2954 (C—H), 1603-1554 (C=C), 1431-1401 (C—O), 1225 (Ar-O-Ar). UV/Vis (DMSO), λ_{max} nm (log ε): 680 (4.80), 613 (4.08), 367 (4.50). ^{1}H NMR (600 MHz, DMSO) δ 8.89 (s, 3H, Ar-H), 8.57–8.25 (s, 3H, Ar-H), 7.78–7.57 (m, 3H, Ar-H), 7.58–7.28 (m, 17H, Ar-H), 7.19–7.05 (m, 2H, Ar-H), 4.02–3.50 (s, 4H, H from COOH), 3.07–2.85 (m, 8H, CH$_2$), 2.98–2.67 (m, 8H, CH$_2$). Anal. Calc. for (C$_{68}$H$_{48}$N$_8$O$_{12}$Zn): C, 66.16; H, 3.92; N, 9.08. Found: C, 65.21: H, 3.56; N, 8.09. MS (MALDI-TOF) m/z: Calcd: 1234.54; Found: 1234.228 [M]$^+$.
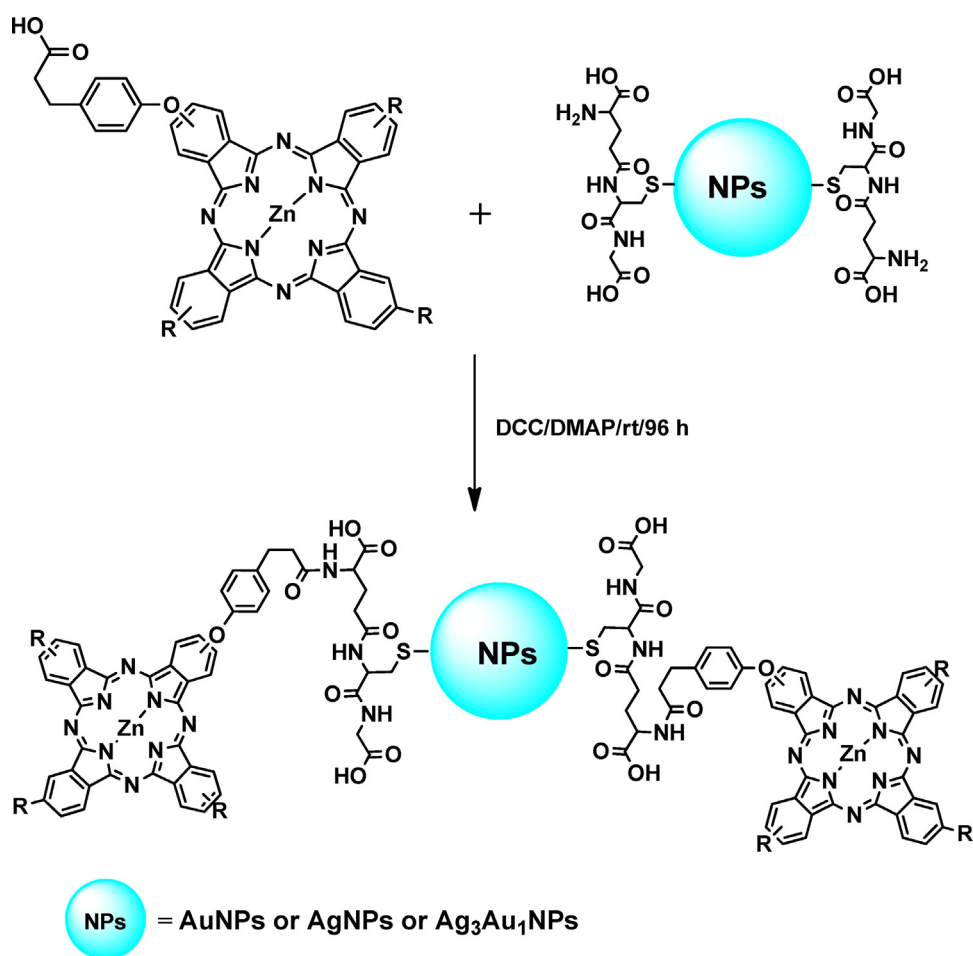
Scheme 3. Synthetic pathways for **2**-AuNPs–GSH, **3**-AuNPs–GSH, **2**-AgNPs–GSH, **3**-AgNPs–GSH, **2**-Ag$_3$Au$_1$NPs–GSH and **3**-Ag$_3$Au$_1$NPs–GSH.
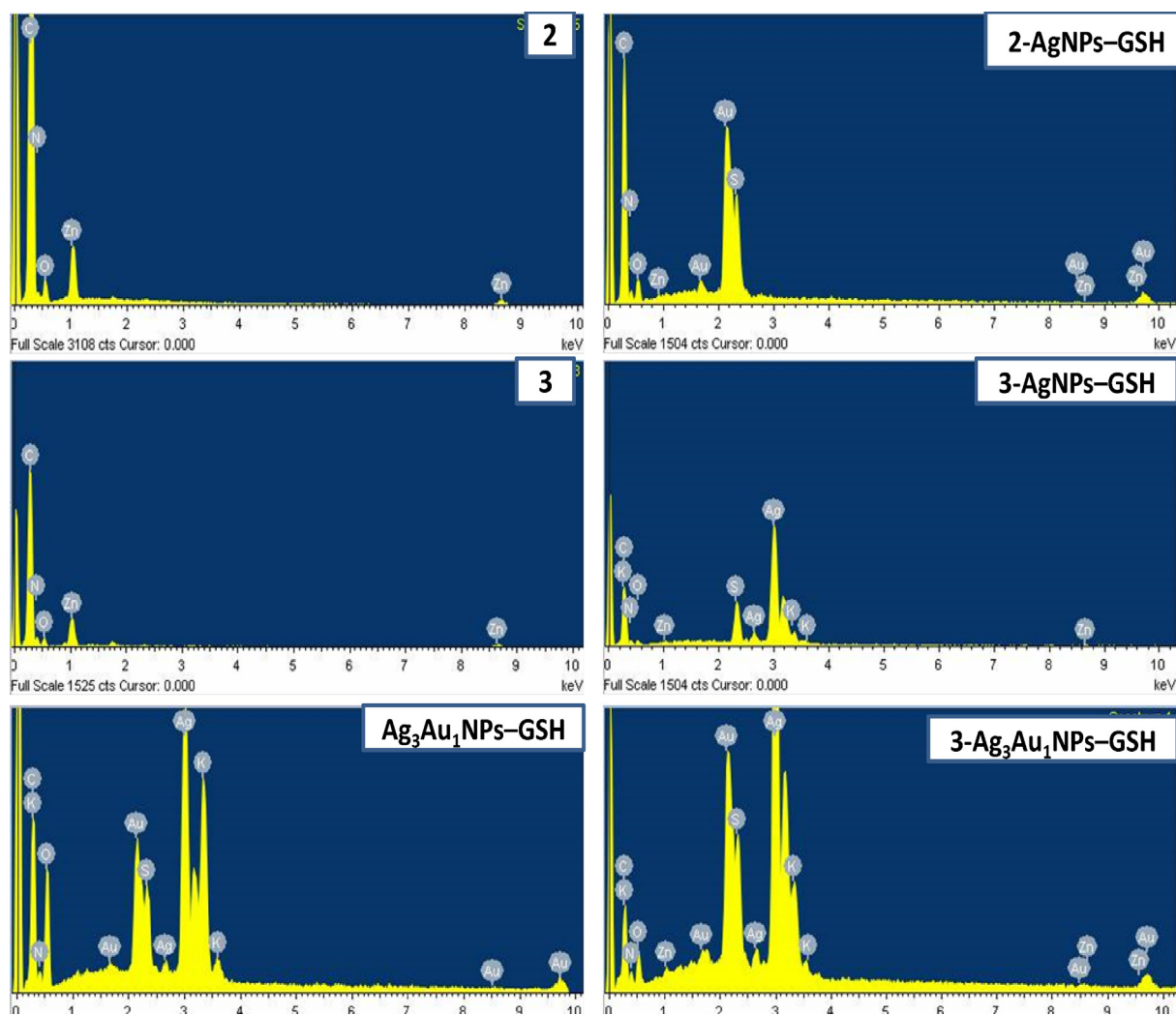
Fig. 5. EDX spectra of complex **2**, **2**-AgNPs–GSH, complex **3**, **3**-AgNPs–GSH, Ag$_3$Au$_1$NPs–GSH and **3**-Ag$_3$Au$_1$NPs–GSH.

2.4.3. Zinc(II) mono–[3–(4–phenoxy) (propanoic acid) phthalocyanine (**3**)

A mixture of 3((4-phenoxy)-propanoic acid) phthalonitrile (**1**) (0.20 g, 0.68 mmol, 1 eq.), 1,2-dicyanobenzene (0.44 g, 3.42 mmol, 5 eq.), zinc (II) acetate dihydrate (0.25 g, 1.1 mmol) and DBU (0.3 mL), dissolved in dry 1-pentanol (3 mL) was refluxed at 180 °C with constant stirring, in the presence of nitrogen for 6 h. The mixture was cooled and washed with methanol several times. Column chromatography was done over silica with THF:methanol (9:1) as an eluent. Several fractions were collected until complex **3** was obtained.

Yield: 0.67 g. IR [νmax/cm^{-1}]: 3204-3020 (COOH), 2912 (C—H stretch), 1701 (—C=O), 1596 (C=C), 1471-1398 (C—OH), 1223 (Ar-O-Ar). UV/Vis (DMSO), λ_{max} nm (log ε): 675 (4.90), 608 (4.46), 356 (4.70). ^{1}H NMR (600 MHz, DMSO) δ 8.25–8.03 (d, *J* = 7.87 Hz, 2H, Ar-H), 7.80–7.62 (d, *J* = 7.73 Hz, 2H, Ar-H), 7.5–7.25 (m, 9H, Ar-H), 7.24–7.04 (m, 6H, Ar-H), 3.55–3.27 (s, 1H, H from COOH), 2.89 (t, *J* = 5.47 Hz, 2H, CH$_2$), 2.73 (t, *J* = 6.21 Hz 2H, CH$_2$). Anal. Calc. for (C$_{41}$H$_{24}$N$_8$O$_3$Zn): C, 66.36; H, 3.26; N, 15.10. Found: C, 65.42: H, 2.89; N, 15.02. MS (MALDI-TOF) *m/z*: Calcd: 742.06; Found: 743.19 [M+H]$^+$.

2.4.4. Covalent linkage of complexes 2 and 3 to NPs

The phthalocyanine–NPs conjugates were synthesized as follows: complex **2** (0.02 g, 0.017 mmol) or complex **3** (0.013 g, 0.017 mmol) were dissolved in 2 mL of dry DMF. Then, DCC (0.01 g, 0.049 mmol) and DMAP (0.005 g, 0.042 mmol) were added and the resulting solution was stirred for 48 h. Afterwards, 0.05 g of the NPs (AuNPs-GSH or AgNPs-GSH or Ag$_3$Au$_1$NPs–GSH) was added and the reaction mixture was stirred for 48 h at room temperature. The conjugates were centrifuged, successively purified with ethanol and allowed to dry in the fume hood. The conjugates are represented as **2**-AuNPs–GSH, **2**-AgNPs–GSH, **2**-Ag$_3$Au$_1$NPs–GSH, **3**-AuNPs–GSH, **3**-AgNPs–GSH and **3**-Ag$_3$Au$_1$NPs–GSH.

2.5. Photophysicochemical studies

Fluorescence (Φ_F) and triplet (Φ_T) quantum yields of complexes **2** and **3**, and their conjugates (**2**-AuNPs–GSH, **2**-AgNPs–GSH, **2**-Ag$_3$Au$_1$NPs–GSH, **3**-AuNPs–GSH, **3**-AgNPs–GSH and **3**-Ag$_3$Au$_1$NPs–GSH) were determined in DMSO and in aqueous media (for Φ_F of the conjugates only) using comparative methods described before in the literatures [32–34].
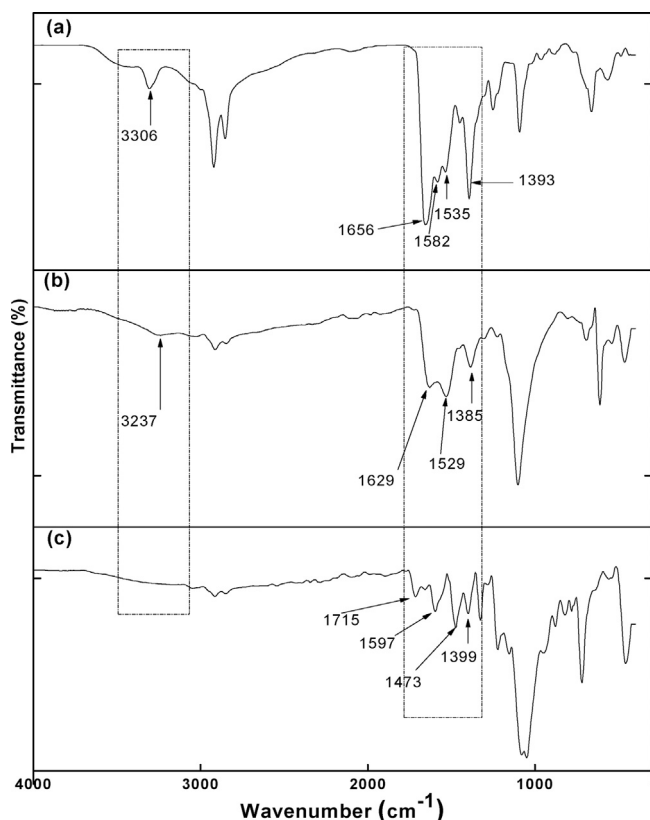
Fig. 6. FT–IR spectra of AuNPs-GSH (a), **3**-AuNPs-GSH (b), complex **3** (c).

Unsubstituted ZnPc in DMSO was used as a standard with $\Phi_F = 0.20$ [33] and $\Phi_T = 0.65$ [34]. The solutions for triplet state studies were de-aerated with argon for 15 min before measurements.

Singlet oxygen quantum yield (Φ_Δ) values were determined under ambient conditions using DPBF as a singlet oxygen quencher in DMSO (and ADMA in water for the conjugates only) and equations described before [35,36]. ZnPc ($\Phi_{\Delta(Std)} = 0.67$) [35] in DMSO and AlPcSmix ($\Phi_{\Delta(Std)} = 0.42$) [37] in water were employed as standards. The absorbances of DPBF or ADMA were spectroscopically monitored at 417 nm or 380 nm, respectively at a predetermined time course.

3. Results and discussion

3.1. Synthesis and characterization of complexes 2 and 3

Schemes 1 and 2, show the synthetic pathway for complexes **2** and **3** respectively. The formation of **1** was via nucleophilic substitution reaction, Scheme 1. Complex **2** was achieved by cyclocondensation of **1** in the presence of DBU, Zn metal salt, and 1-pentanol. The formation of **3** was by cross–condensation of **1** and dicyanobenzene in the presence of DBU, Zn metal salt, and 1-pentanol. The disappearance of $C\equiv N$ peak at 2230 cm^{-1} observed for compound **1** in the FT-IR spectra of **2** and **3** confirmed the formation of complexes. The ^1H NMR spectrum for **2** contains aromatic ring proton peaks between 8.89−7.05 ppm, and between 8.25−7.04 ppm for complex **3**. The proton of the COOH resonates between 4.02–3.27 ppm for complexes **2** and **3**, while the CH$_2$ of

the propanoic acid chain was observed between 3.07−2.67 ppm. Peak integration gave the anticipated total number of protons, confirming the relative purity of the complexes. Mass spectral data and elemental analyses were in agreement with the proposed structures in Schemes 1 and 2.

The UV–vis spectra of both complexes **2** and **3** in DMSO are shown in Fig. 1. The electronic ground state absorption spectra provide no evidence of band broadening due to aggregation and contain a single Q band at 680 and 675 nm, for complexes **2** and **3**, respectively (Table 1), which is what is typically observed for metalated phthalocyanine with degenerate D$_{4h}$ symmetry [38]. The red shift in the Q band of complex **2** compared to **3**, can be attributed to a decrease in energy gap between the highest occupied molecular orbital (HOMO) and lowest unoccupied molecular orbital (LUMO) of complex **2** as described below.

The theory of MCD is based on the analyses of the three Faraday terms, **A$_1$**, **B$_0$** and **C$_0$**, which provide information on state degeneracies and band polarizations that cannot be derived from the UV–vis absorption spectrum alone [39]. The MCD spectra of complexes **2** (Fig. 2) and **3** (Fig. S2, ESI) are similar to what would normally be expected for a monomeric ZnPc since intense A$_1$ or pseudo-A$_1$ terms are observed in the Q and B-band regions with cross-over points at 681 nm and 355 nm, respectively, corresponding to the absorption band maxima for complex **2** [39], as would be anticipated for transitions to degenerate or near degenerate excited states. Complex **3** also showed similar behaviour with cross over point at 675 nm and 348 nm, for the Q and B bands, respectively.

From the MCD spectroscopy, we can therefore unambiguously assign the 680 and 355 nm pseudo-**A$_1$** terms to the Q and B transitions, respectively, in accordance with Gouterman's four-orbital model [40] for complex **2**. In a similar manner, 675 and 348 nm can be assigned as the Q and B transitions for complex **3**. The predicted TD-DFT spectra for complexes **2** and **3** (Figs. 2 and S2, ESI) were found to be consistent with this assignment, since intense x- and y- or x/y-polarized bands are predicted in the Q band region that are dominated by the one-electron transitions between the HOMO and the LUMO and LUMO + 1, which correspond to the 1a$_{1u}$ and 1e$_g$* MOs of Gouterman's four-orbital model [40], while intense bands predicted in the B band regions have significant contributions from the MO (molecular orbital) corresponding to the 1a$_{2u}$ MO (Table S1).

A slight narrowing of the HOMO–LUMO gap is predicted for complex **2** compared to **3** (Fig. 3) due to a relative destabilization of the HOMO, which accounts for the red shift which is observed for the Q band of complex **2**. The HOMO has large MO coefficients on all eight of the peripheral carbons that form the potential points of attachment for the peripheral substituents, while only four of these atoms have large MO coefficients in the context of the LUMO and LUMO + 1, so the mesomeric effects associated with the lone pairs on the oxygen atoms (Fig. S3, ESI) can have a larger destabilizing effect on the HOMO. The envelopes of intensity observed in each case to the red of the B band (Figs. 2 and S2, ESI) can be attributed in each case to transitions from π-MOs with large MO coefficients on the peripheral fused benzo rings that are destabilized through similar mesomeric interactions with the peripheral substituents into the LUMO and LUMO + 1 [39].

The absorption, excitation and emission spectra are shown in Fig. 4 (complex **3** as a representative) in DMSO. It can be seen that the emission spectra were mirror images of the excitation spectra and the latter was close to the absorption spectra, indicating a non-aggregation of phthalocyanine in solution. The closeness of the Q-band absorption maxima to that of excitation shows that the ground state nuclear configuration of complex **3** was not affected by excitation.
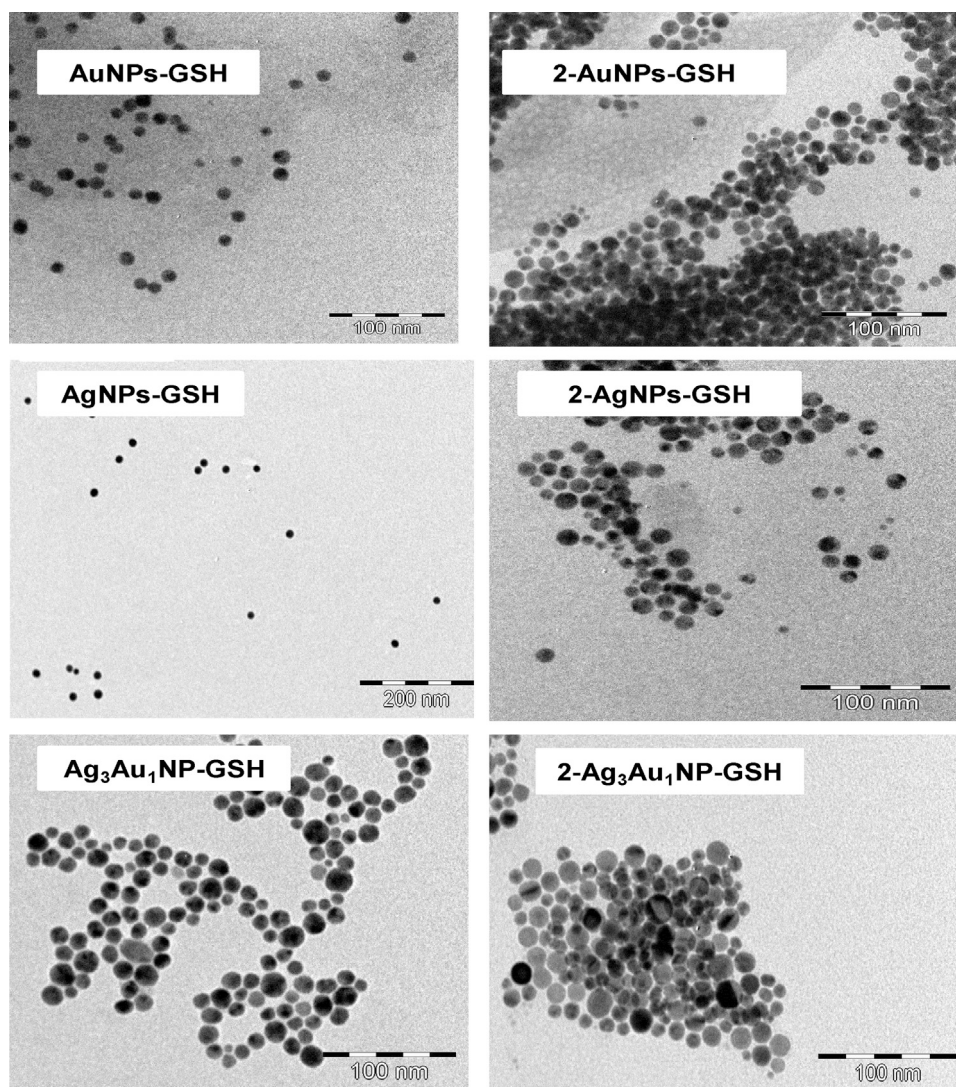
Fig. 7. Representative TEM micrographs for glutathione functionalized AuNPs, AgNPs, Ag$_3$Au$_1$NPs and when conjugated to complex **2**.

## 3.2. Synthesis and characterization of the conjugates

3.2.1. Synthesis

The activated —COOH terminal end of complexes **2** and **3** was covalently coupled with the —NH$_2$ group of the GSH functionalized NPs to form amide bond using DCC and DMAP as coupling agents, Scheme 3.

Since the approximate size of the Pc is approximately 1 nm and that of the NPs are greater than 10 nm (see Table 1 and the discussion below), there is high probability that more than one Pc will be bound to the NPs from size consideration. The loading of complexes **2** and **3** onto the nanoparticles was investigated following literature methods [41]. This involves comparing the Q band absorbance intensity of the Pc in the conjugate with that of the initial Pc before the conjugation. The loadings of Pc onto nanoparticles are listed in Table 1. It was found that there were a larger number of Pcs that are loaded onto Ag$_3$Au$_1$NPs-GSH than AuNPs-GSH and AgNPS-GSH, which could be attributed to increased size (to be determined below, see also Table 1) of the Ag$_3$Au$_1$NPs-GSH resulting in more available active sites for attachment.

The elemental compositions of the complexes and conjugates were qualitatively determined using an energy dispersive X-ray spectrometer (EDX) as shown in Fig. 5. The EDX spectra of the complexes **2** and **3**, showed the presence of C, N, O and Zn, which are the expected elements for the Pcs. Upon conjugation to the glutathione functionalized nanoparticles, the spectrum display additional elements, Ag and S for silver conjugates, Au and S for the corresponding gold conjugates and Ag, Au and S for the silver-gold alloy conjugates. The presence of sulphur in the conjugates comes from the glutathione used to functionalize the nanoparticles. The AgNPs-GSH and Ag$_3$Au$_1$NPs-GSH conjugates show the presence of residual potassium from KOH used during glutathione functionalisation of the NPs.

FTIR spectra were employed to prove amide bond formation between the Pc complexes and the NPs, Fig. 6 using AuNPs-GSH, **3**-AuNPs-GSH and complex **3**, as examples. The MPc complexes and GSH (in the NPs) have hydroxyl groups from carboxylic acid, shown by broadening from 3020 cm^{-1} to about 3400 cm^{-1}. These overlap with the NH peaks from GSH as shown by an intense NH peak at 3306 cm^{-1} in AuNPs-GSH as an example (Fig. 6a). The shift in the position of the NH peak to 3237 cm^{-1} in **3**-AuNPs-GSH (Fig. 6b)
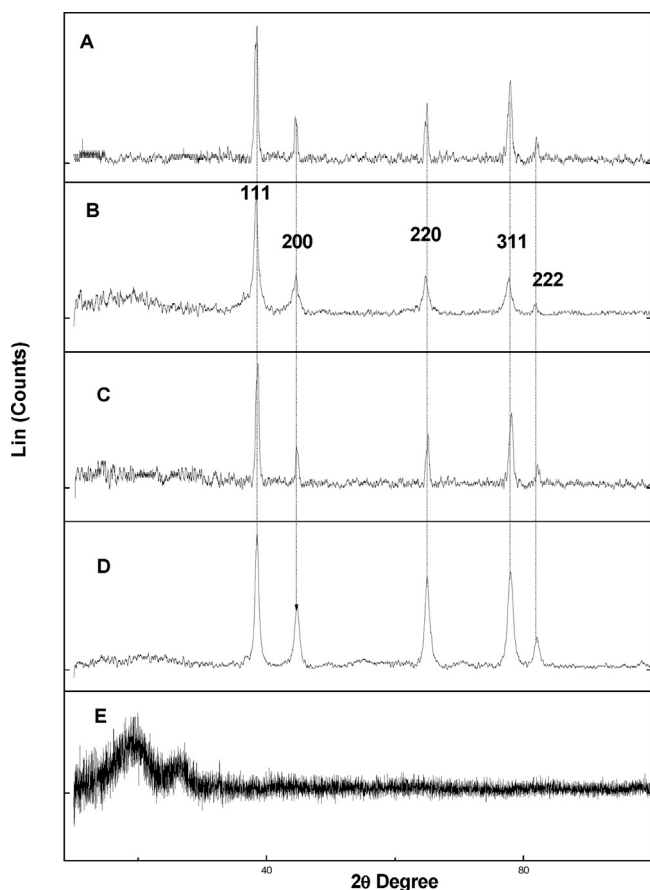
Fig. 8. XRD diffractograms for AgNPs-GSH (A), **2**-AgNPs–GSH (B), AuNPs–GSH (C), **3**-AuNPs–GSH (D) and complex **2** (E).

shows the involvement of these groups in the formation of the amide bond. Shifts in the IR bands confirm structural change [42].

Split peaks at 1582 cm^{-1} and 1535 cm^{-1} in the GSH functionalized nanoparticles alone are typical of primary amines. The disappearance of the primary amine peak (at 1582 cm^{-1}) in AuNPs-GSH and the carboxylic acid carbonyl peak (at 1715 cm^{-1}) in complex **3**, upon formation of **3**-AuNPs-GSH, as well as the emergence of a peak at 1629 cm^{-1} (amide band, O=C—NH) in **3**-AuNPs-GSH, suggest a linkage of the glutathione functionalised nanoparticles to complex **3** through the amide bond. It should be noted that GSH alone has amide bonds shown by a peak at 1656 cm^{-1} in AuNPS-GSH, shifted compared to 1629 cm^{-1} in **3**-AuNPs-GSH. The same trend was observed for the other conjugates (**2**-AgNPs–GSH, **2**-AuNPs–GSH, **3**-AgNPs–GSH, **2**-Ag$_3$Au$_1$NPs–GSH and **3**-Ag$_3$Au$_1$NPs–GSH).

The TEM micrographs for AuNPs–GSH, AgNPs–GSH, **2**–AuNPs–GSH, **2**-AgNPs–GSH, and **2**-Ag$_3$Au$_1$NPs–GSH are shown as examples in Fig. 7. The NPs alone were relatively monodispersed however upon conjugation, slight aggregation was observed probably due, to interactions between the Pcs on adjacent NPs via π-π stacking since Pcs are known for their π-π stacking to form H aggregates [43].

Fig. 8 shows the X-ray diffraction (XRD) pattern of the silver and gold nanoparticles, and their conjugates (AgNPs-GSH, AuNPs-GSH, **2**, **2**-AgNPs-GSH and **3**-AuNPs-GSH are used as examples). The XRD diffraction patterns of the nanoparticles showed well-defined crystalline peaks assigned to the 111, 200, 220, 311 and 222 planes, corresponding to the face centered-cubic structures of metallic gold and silver [44,45]. The XRD patterns of complexes **2** and **3** contains broad peaks between 2θ = 17–25°, which is consistent

with the amorphous nature of phthalocyanines [46]. Upon conjugation to form conjugates, slight broadening was observed in this region, which provides evidence for the presence of the phthalocyanine.

Debye-Scherrer Eq. (1) [47] was employed for the estimation of the sizes of the NPs:

$$d = \frac{k\lambda}{\beta COS\theta} \quad (1)$$

where λ is the wavelength of the X-ray source (1.5405 Å), k is an empirical constant equal to 0.9, β is the full width at half maximum of the diffraction peak and θ is the angular position. The sizes were estimated to be 11.1 nm (AgNPs-GSH), 13.6 nm (AuNPs-GSH), 15.1 nm (Ag$_3$Au$_1$NPs-GSH), 14.7 nm (**2**-AgNPs–GSH), 12.2 nm (**3**-AgNPs–GSH), 14.9 nm (**2**-AuNPs–GSH), 13.8 nm (**3**-AuNPs–GSH), 17.3 nm (**2**-Ag$_3$Au$_1$NPs–GSH) and 16.5 nm **3**-Ag$_3$Au$_1$NPs–GSH, Table 1. There is an increase in the size of the NPs upon coordination to the Pcs, most likely due to aggregation as discussed above.

Fig. 9 shows a selection of UV–vis spectra of the glutathione functionalized nanoparticles and their conjugates with MPc complexes. A general red shift in the surface plasmon resonance (SPR) band of the metallic nanoparticles was observed upon linking of complexes **2** and **3** to the nanoparticles, indicating an increase in size following conjugation. The SPR peak for **3**-AgNPS-GSH (Fig. 9C) was observed at 432 nm and at 426 nm for **2**-AgNPS-GSH (Fig. 9B) compared to 405 nm (Fig. 9A) for AgNPS-GSH alone, Table 1. Thus both conjugates show red shifts compared to AgNPs-GSH alone. **3**-AuNPS-GSH showed the SPR band at 530 nm and **2**-AuNPS-GSH at 542 nm compared to 532 nm for AuNPs-GSH alone. Thus there is a slight blue shift for **3**-AuNPS-GSH and a clear red shift for **2**-AuNPS-GSH. For **2**-Ag$_3$Au$_1$NPs–GSH and **3**-Ag$_3$Au$_1$NPs–GSH only the AgNPs SPR bands were clear with red shifts to 443 nm and ∼440 nm respectively, compared to Ag$_3$Au$_1$NPs–GSH alone at 408 nm. The observation of mainly AgNPs SPR band in Ag$_3$Au$_1$NPs–GSH is due the larger amount of Ag vs Au in the composite. Red shifts in SPR bands may be due to aggregation.

The presence of SPR peaks in the conjugates confirms successful linkage of the complex to nanoparticles. Pertinent to note, is that the complexes maintain their Q band absorption peak after conjugation. There were no shifts in the Q band of complexes **2** and **3** following conjugation, Table 1.

In aqueous media (Fig. S4, ESI), the complexes and their conjugates show broad bands with higher energy bands being due to aggregation typical of Pcs in aqueous solution [43] resulting from π–π stacking interaction of the aromatic rings of Pcs. The Q bands are very weak for the conjugates in water, but the SPR band is still observable for AuNPs, AgNPs, and Ag$_3$Au$_1$NPs conjugates.

3.3. Photophysicochemical parameters

Table 1 compares the fluorescence quantum yields (Φ_F) and lifetimes (τ_F), triplet quantum yields (Φ_T) and lifetimes (τ_T), and singlet oxygen quantum yields (Φ_Δ) of complexes **2** and **3** alone, and their conjugates using DMSO (and in some cases water in brackets) as a solvent.

3.3.1. Fluorescence quantum yields (Φ_F) and lifetimes (τ_F)

A typical fluorescence decay profile for complex **2** is shown in Fig. 10 (as an example). A mono-exponential decay profile indicating one life-time was obtained for all the complexes.

As shown in Table 1, there was a decrease in the fluorescence quantum yields of complexes **2** and **3** on conjugation to NPs, indicating a significant quenching of the excited singlet state of the complexes, due to the heavy atom effect which promotes
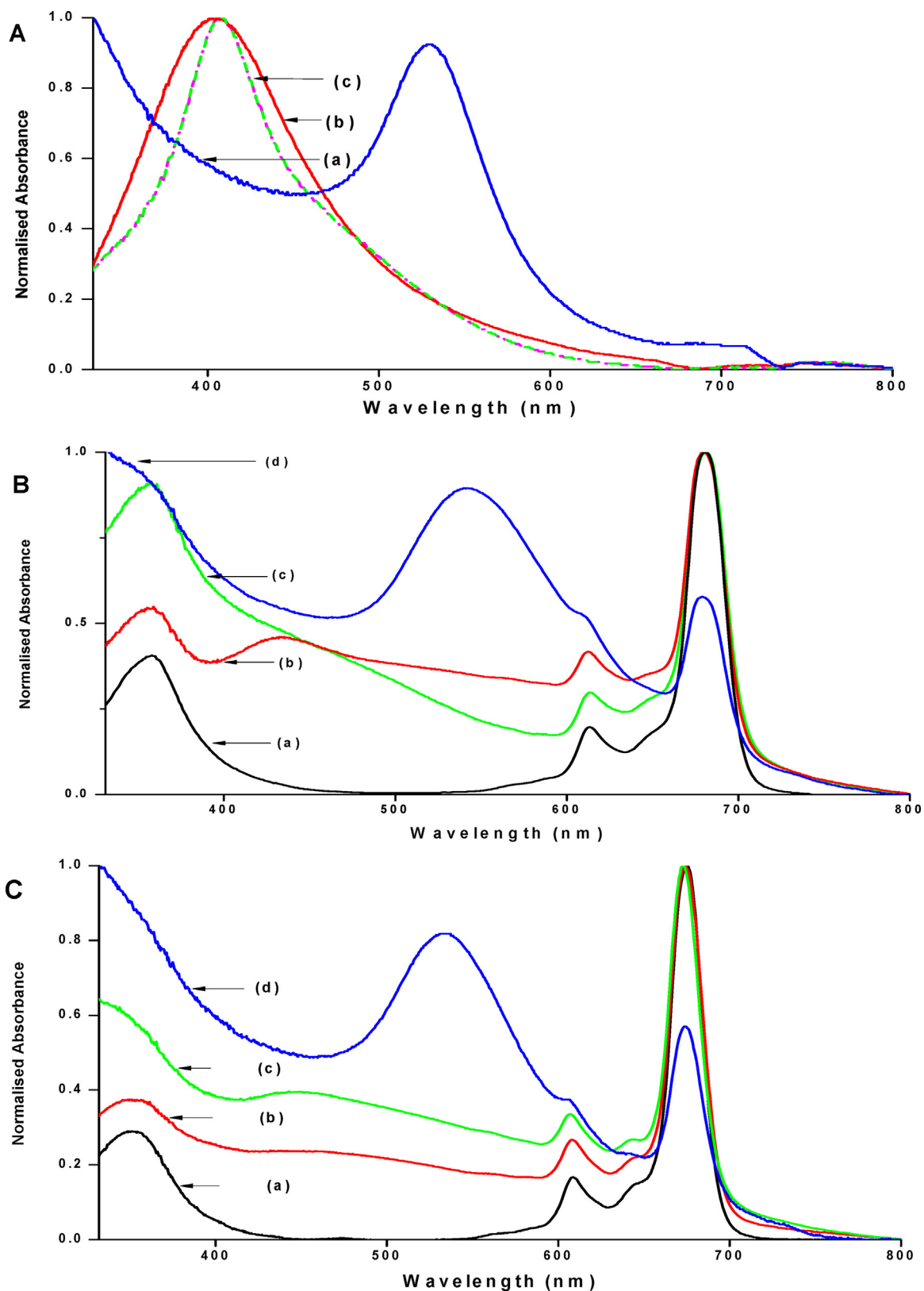
Fig. 9. Absorption spectra of (A) AuNPs-GSH (a), AgNPs-GSH (b) and Ag$_3$Au$_1$NPs–GSH (c) (solvent = water); (B) **2** (a), **2**-AgNPs (b), **2**-Ag$_3$Au$_1$NPs–GSH (c) and **2**-AuNPs (d), and (C) **3** (a), **3**-AgNPs (b), **3**-Ag$_3$Au$_1$NPs–GSH (c) and **3**-AuNPs (d) (solvent = DMSO).

intersystem crossing to the triplet state. It should be noted however that other non-radiative pathway such as internal conversion can also have a significant contribution towards the decrease in fluorescence quantum yields.

The fluorescence lifetimes also decreased following conjugation as expected since fluorescence quantum yields and lifetimes have a direct relationship. However it should be noted that there was a significant decrease in Φ_F compared to τ_F.
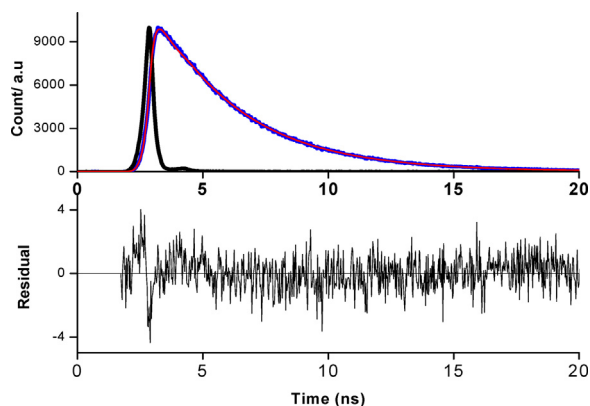
Fig. 10. Fluorescence decay (blue), χ^2 fitting (red) and instrument response function (IRF, black) curves for complex **2** in DMSO. (For interpretation of the references to colour in this figure legend, the reader is referred to the web version of this article.)

Following the kinetic model, the absorption coefficients and excited state lifetimes are directly related to the radiative lifetime (τ_0) hence these were determined using the measured fluorescence quantum yield (Φ_F) and lifetime (τ_F) as shown in Eq. (2) [48]

$$\tau_0 = \frac{\tau_F}{\Phi_F} \qquad (2)$$

All the complexes and the corresponding conjugates having high radiative lifetime (Table 1) showed lower fluorescence quantum yield in accordance with the model. Thus, the decrease in fluorescence quantum yields can be significantly higher than for the corresponding fluorescence lifetimes.

The fluorescence quantum yields decreased when the study was carried out in water compared to DMSO, which could be attributed to aggregation since aggregates do not fluoresce. The presence of aggregates has been reported to decrease quantum yield through the conversion of electronic excitation energy of fluorophores to vibrational energy [49].

Faster intersystem crossing lifetime will result in higher triplet quantum yield. The intersystem crossing lifetimes (τ_{isc}) (calculated using $\tau_{isc} = \tau_F/\Phi_T$) are presented in Table 1. The intersystem crossing lifetimes range from 3.42 ns to 6.22 ns. The conjugates showed shorter τ_{isc} values than the Pc complexes, which indicates

Fig. 11. Triplet absorption decay (black) and fitting (red) curves for complex **2** in DMSO. (For interpretation of the references to colour in this figure legend, the reader is referred to the web version of this article.)
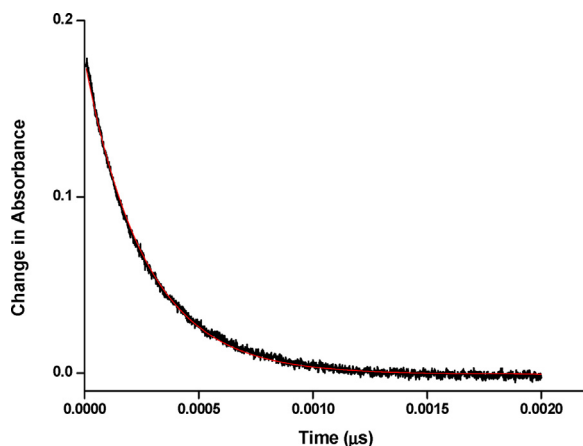
faster intersystem crossing to the triplet resulting in higher triplet quantum yield.

3.3.2. Triplet quantum yields (Φ_T) and lifetimes (τ_T)

An ideal photosensitizer is expected to have high triplet state quantum yield. Higher triplet quantum yield can only be possible if the intersystem crossing lifetime is less than the triplet lifetime, which will result in the population of the triplet state. This is the case in Table 1.

The triplet decay curve of complex **2** is shown in Fig. 11 (as an example) and all the Pcs and conjugates were found to obey second order kinetics, which is typical of MPcs complexes at high concentration, due to triplet-triplet recombination [50,51]. The low symmetry complex **3** showed higher triplet quantum yield than the tetra substituted complex **2**, which is in agreement with the literature report that low symmetry phthalocyanines possess better photophysical behaviour than their corresponding symmetrical analogue [52]. The increase in triplet quantum yield observed upon conjugation of complexes **2** and **3** to metallic nanoparticles (Table 1) corresponds to the decrease in fluorescence quantum yield as expected since the two processes have an inverse relationship. The enhancement of the triplet quantum yield could be attributed to the promotion of intersystem crossing to the triplet state resulting due to the heavy atom effect of gold and silver heavy atoms in the nanoparticles.

Conjugates containing Au (a heavier atom than Ag), as expected have larger Φ_T values compared to the Ag counterparts. The **3**-Ag$_3$Au$_1$-GSH gave a lower Φ_T when compared to **3**-AuNPS-GSH but was similar to **3**-AgNPS-GSH. For **2**-AuNPS-GSH, **2**-AgNPS-GSH and **2**-Ag$_3$Au$_1$NPs, there were only slight differences in Φ_T values. It is also possible that the Pc loading on the NPs affect their excited state parameters. Ag$_3$Au$_1$NPs conjugates with the largest loadings gave lower Φ_T values than AgNPs conjugates with the lower loading, probably due to aggregation in the former, which will result in quenching.

High Φ_T values are usually accompanied by short triplet lifetimes, however in this case longer triplet lifetimes were obtained suggesting the protection of the MPc complexes by AgNPs-GSH/AuNPs-GSH since the NPs are much larger than the Pc at ∼1 nm [53,54]. Both complexes and their conjugates displayed reasonably high Φ_T, making them suitable for all applications that require a high Φ_T.

3.3.3. Singlet oxygen quantum yields

Efficient interaction of the triplet state of photosensitizer with the ground state molecular oxygen can result in generation of singlet oxygen due to energy transfer from the photosensitizer to the molecular oxygen. In order to determine the singlet oxygen quantum yield (Φ_Δ), the chemical photodegradation of the singlet oxygen quencher (DPBF) in DMSO (using complex **3** as an example) and ADMA in water (using **3**-Ag$_3$Au$_1$NPS-GSH as an example) was monitored over a period of time (Fig. 12). Irradiation at the Q-band showed the stability of the complexes over the irradiation period, while DPBF and ADMA degraded (minimally for the latter). A significant increase in singlet oxygen generation was observed as evidenced by singlet oxygen quantum yield (Table 1) upon conjugation of complex **2** and **3** to the silver and gold nanoparticles corresponding to an increase in triplet quantum yield. Even though the conjugates of Ag$_3$Au$_1$NPs–GSH displayed increased triplet quantum yields, they afforded lower singlet oxygen quantum yield than the MPc complexes alone. The lower singlet oxygen quantum yield could probably be due to the screening effect caused by the NPs, which could have prevented the interaction of the excited triplet state of the conjugates and the ground state molecular oxygen [55–57], which would be more severe for the larger Ag$_3$Au$_1$NPs–GSH conjugates. Thus, AgNPs or AuNPs alone may be
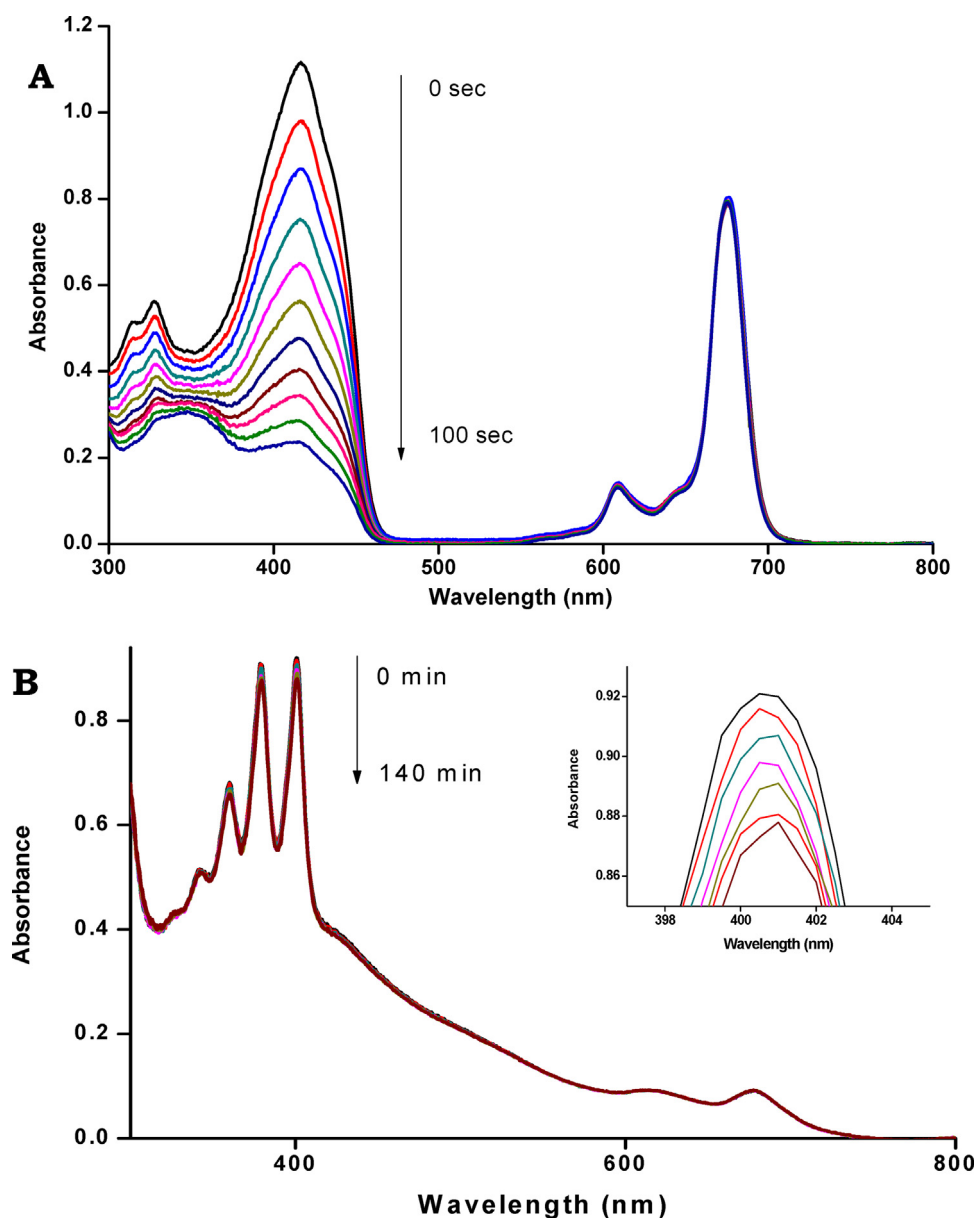
Fig. 12. UV–vis spectra showing the degradation of (A) DPBF (9.0×10^{-6}M) in the presence of complex **3** (5.2×10^{-5}M) in DMSO and (B) ADMA (4.5×10^{-5}M) in the presence of **3**-Ag$_3$Au$_1$NPs-GSH (1.3×10^{-6}M) in water.

preferable over the amalgam for improved singlet oxygen, depending on the size of the NPs. Values are low in water due to aggregation. In addition, water is known to quench the singlet state [33].

High singlet oxygen quantum yields generation makes these complexes and the corresponding conjugates potential materials for photodynamic therapy and photocatalysis.

4. Conclusion

In this work, we report on the synthesis of zinc(II) tetra–[3-(4-phenoxy) propanoic acid) phthalocyanine] (complex **2**) and zinc(II) mono–(4-phenoxy) propanoic acid) phthalocyanine (complex **3**) which were characterised using FTIR, UV–vis, ^{1}HNMR, MALDI-TOF mass spectroscopies and elemental analyses. The MPcs were covalently linked to AgNPs-GSH, AuNPs-GSH and Ag$_3$Au$_1$NPs–GSH, and the conjugates formed were characterized using XRD, TEM, UV/vis, FT-IR spectrometer and EDX. The photophysichochemical

behaviour of the MPcs and their conjugates were also studied. The conjugates displayed improved triplet and singlet quantum yields than MPcs alone, with the exception of the Ag$_3$Au$_1$NPs–GSH conjugates which afforded lower singlet quantum yields.

Appendix A. Supplementary data

Supplementary data associated with this article can be found, in the online version, at http://dx.doi.org/10.1016/j.jphotochem.2017.09.020.

References

[1] I. Okura, Photosensitization of Porphyrins and Phthalocyanines, Gordon and Breach Publishers, Germany, 2001.

[2] P. Gregory, High-Technology Applications of Organic Colourant, Plenum Press, New York, 1991.

[3] N. Kuznetsova, E.A. Makarova, S.N. Dashkevich, N.S. Gretsova, E.A. Kalmykova, V.M. Negrimovsky, O.L. Kaliya, E.A. Lukyanets, Structure-photochemical properties relationship for porphyrins and related compounds, Russ. J. Gen. Chem. 70 (2000) 140–148.

[4] T. Nyokong, Desired properties of new phthalocyanines for photodynamic therapy, Pure Appl. Chem. 83 (2011) 1763–1779.

[5] A.W. Snow, Porphyrin handbook, in: K.M. Kadish, K.M. Smith, R. Guilard (Eds.), Phthalocyanine Properties and Materials, Academic Press, New York, 2003 (Chapter 109).

[6] M. Hanack, T. Schneider, M. Barthel, J.S. Shirk, S.R. Flom, R.G.S. Pong, Indium phthalocyanines and naphthalocyanines for optical limiting, Coord. Chem. Rev. 219 (2001) 235–258.

[7] A. Zawadzka, P. Plociennik, J. Strzelecki, M. Pranaitis, S. Dabos-Seignon, B. Sahraoui, Structural and nonlinear optical properties of as- grown and annealed metallophthalocyanine thin films, Thin Solid Films 545 (2013) 429–437.

[8] A. Zawadzka, P. Plociennik, J. Strzelecki, A. Korcala, A.K. Arof, B. Sahraoui, Impact of annealing process on stacking orientations and second order nonlinear optical properties of metallophthalocyanine thin films and nanostructures, Dyes Pigment 101 (2014) 212–220.

[9] A. Zawadzka, A. Karakas, P. Plociennik, J. Szatkowski, Z. Lukasiak, A. Kapceoglu, Y. Ceylan, B. Sahraoui, Optical and structural characterization of thin films containing metallophthalocyanine chlorides, Dyes Pigment 112 (2015) 116–126.

[10] S. Zongo, M.S. Dhlamini, P.H. Neethling, A. Yao, M. Maaza B. Sahraoui, Synthesis, characterization and femtosecond nonlinear saturable absorption behavior of copper phthalocyanine nanocrystals doped-PMMA polymer thin films, Opt. Mater. 50 (2015) 138–143 Part: B.

[11] R. Bonnett, Chemical Aspects of Photodynamic Therapy, Gordon and Breach Science Publishers, Amsterdam, 2000.

[12] S.B. Brown, E.A. Brown, I. Walker, The present and future role of photodynamic therapy in cancer treatment, Lancet. Oncol. 5 (2004) 497–508.

[13] M. Idowu, T. Loewenstein, A. Hastall, T. Nyokong, D. Schlettwein, Photoelectrochemical properties of electrodeposited ZnO thin films sensitized by octacarboxymetallophthalocyanine derivatives, J. Porphyr. Phthalocyanines 14 (2010) 142–149.

[14] B.C. De Simone, G. Mazzone, N. Russo, E. Sicilia, M. Toscano, Metal atom effect on the photophysical properties of Mg(II) Zn(II), Cd(II), and Pd(II) tetraphenylporphyrin complexes proposed as possible drugs in photodynamic therapy, Molecules 22 (2017) 1093.

[15] Y. Shimzu, T. Azumi, Mechanism of external heavy atom effect on intersystem crossing in fluid solutions. Analysis based on fluorescence decay data, J. Phy. Chem. 86 (1982) 22–26.

[16] O.M. Bankole, O. Osifeko, T. Nyokong, Enhanced nonlinear optical responses of zinc diaminopyrimidin-2-ylthio phthalocyanine conjugated to Ag_xAu_yalloy nanoparticles, J. Photochem. Photobio. A: Chem. 329 (2016) 155–166.

[17] A. Taglietti, Y.A. Diaz-Fernandez, E.D. Amato, L. Cucca, G. Dacarro, M.E. Wieder, D.C. Hone, M.J. Cook, M.M. Handsley, J. Gavrilovic, D.A. Russell, Intracellular photodynamic therapy with photosensitizer-nanoparticle conjugates: cancer therapy using a 'Trojan horse, Photochem. Photobiol. Sci. 5 (2006) 727–734.

[18] P. Grisoli, V. Necchi, P. Pallavicini, L. Pasotti, M. Patrini, Antibacterial activity of glutathione-coated silver nanoparticles against gram positive and gram negative bacteria, Langmuir 28 (2012) 8140–8148.

[19] N. Masilela, T. Nyokong, Conjugates of low-symmetry Ge, Sn and Ti carboxy phthalocyanines with glutathione caped gold nanoparticles: an investigation of photophysical behaviour, J. Photochem. Photobiol. A: Chem. 223 (2011) 124–131.

[20] M. Camerin, M. Magaraggia, M. Soncin, G. Jori, G.M. Moreno, I. Chambrier, M.J. Cook, D.A. Russell, The in vivo efficacy of phthalocyanine–nanoparticle conjugates for the photodynamic therapy of amelanotic melanoma, Eur. J. Cancer 46 (2010) 1910–1918.

[21] N. Nombona, K. Maduray, E. Antunes, A. Karsten, T. Nyokong, Synthesis of phthalocyanine conjugates with gold nanoparticles and liposomes for photodynamic therapy, J. Photochem. Photobiol. B: Biol. 107 (2012) 35–44.

[22] N. Nombona, E. Antunes, C. Litwinski, T. Nyokong, Synthesis and photophysical studies of phthalocyanine–gold nanoparticle conjugates, Dalton Trans. 40 (2011) 11876–11884.

[23] T.P. Mthethwa, S. Tuncel, M. Durmuş, T. Nyokong, Photophysical and photochemical properties of a novel thiol terminated low symmetry zinc phthalocyanine complex and its gold nanoparticles conjugate, Dalton Trans. 42 (2013) 4922–4930.

[24] N. Masilela, T. Nyokong, The interaction of silver nanoparticles with low symmetry cysteinyl metallophthalocyanines and their antimicrobial effect, J. Photochem. Photobiol. A: Chem 255 (2013) 1–9.

[25] E. Dube, D.O. Oluwole, T. Nyokong, Photophysicochemical behaviour of anionic indium phthalocyanine when grafted onto Ag_xAu_y and porous silica nanoparticles, J. Luminesc. 190 (2017) 353–363.

[26] M. Ambroz, A. Beeby, A.J. McRobert, M.S.C. Simpson, R.K. Svensen, D. Phillips, Preparative, analytical and fluorescence spectroscopic studies of sulphonated aluminium phthalocyanine photosensitizers, J. Photochem. Photobiol. B: Biol. 9 (1991) 87–95.

[27] J.G. Young, W. Onyebuagu, Synthesis and characterization of di-disubstituted phthalocyanines, J. Org. Chem. 55 (1990) 2155–2159.

[28] A. Fashina, E. Antunes, T. Nyokong, Characterization and photophysical behavior of phthalocyanines when grafted onto silica nanoparticles, Polyhedron 53 (2013) 278–285.

[29] M. Decker, M.W. Klein, M. Wegener, S. Linden, Circular dichroism of planar chiral magnetic metamaterials, Opt. Lett. 32 (2007) 856–858.

[30] M.J. Frisch, G.W. Trucks, H.B. Schlegel, G.E. Scuseria, M.A. Robb, G. Cheeseman, J.R. Scalmani, V. Barone, B. Mennucci, H. Petersson, G.A. Nakatsuji, M. Caricato, X. Li, H.P. Hratchian, A.F. Izmaylov, J. Bloino, G. Zheng, J.L. Sonnenberg, K. Hada, M. Ehara, M. Toyota, R. Fukuda, J. Hasegawa, M. Ishida, T. Nakajima, Y. Honda, O. Kitao, H. Nakai, T. Vreven, J.E. Montgomery, J.A. Peralta, F. Ogliaro, M. Bearpark, J.J. Heyd, E. Brothers, K.N. Kudin, R. Staroverov, V.N. Kobayashi, K. Normand, J. Raghavachari, A. Rendell, J.C. Burant, S.S. Iyengar, J. Tomasi, M. Cossi, N. Rega, J. M. Millam, M. Klene, J.E. Knox, J.B. Cross, V. Bakken, C. Adamo, J. Jaramillo, R. Gomperts, R.E. Stratmann, O. Yazyev, A.J. Austin, R. Cammi, C. Pomelli, J.W. Ochterski, R.L. Martin, K. Morokuma, V.G. Zakrzewski, G.A. Voth, P. Salvador, S. Dannenberg, J.J. Dapprich, A.D. Daniels, O. Farkas, J.B. Foresman, J.V. Ortiz, J. Cioslowski, D.J. Fox, Gaussian 09, Revision E. 01, Gaussian, 2009.

[31] R.J. Magyar, S. Tretiak, Dependence of spurious charge-transfer excited states on orbital exchange in TDDFT: Large molecules and clusters, J. Chem. Theory Comput. 3 (2007) 976–987.

[32] S. Fery-Forgues, D. Lavabre, Modified mesoporous silica nanoparticles as a reusable, selective chromogenic sensor for mercury (II) recognition, J. Chem. Educ. 76 (1999) 1260–1264.

[33] A. Ogunsipe, J.Y. Chen, T. Nyokong, Photophysical and photochemical studies of zinc (II) phthalocyanine derivatives–effects of substituents and solvents, New J. Chem. 28 (2004) 822–827.

[34] T.H. Tran-Thi, C. Desforge, C. Thiec, S.J. Gaspard, Singlet?singlet and triplet–triplet intramolecular transfer processes in a covalently linked porphyrin–phthalocyanine heterodimer, J. Phys. Chem. 93 (1989) 1226–1233.

[35] N.A. Kuznetsova, N.S. Gretsova, O.A. Yuzhakova, V.M. Negrimovskii, O.L. Kaliya, E.A. Luk'yanets, New reagents for determination of the quantum efficiency of singlet oxygen generation in aqueous media, Russ. J. Gen. Chem. 71 (2001) 36–41.

[36] W. Spiller, H. Kliesch, D. Wohrle, S. Hackbarth, B. Roder, G. Schnurpfeil, Singlet oxygen quantum yields of different photo-sensitizers in polar solvents and micellar solutions, J. Porphyrins Phthalocyanines 2 (1998) 145–158.

[37] T. Nyokong, E. Antunes, Chapter title: photochemical and photophysical properties of metallophthalocyanines, in: K.M. Kadish, K.M. Smith, R. Guilard (Eds.), The Handbook of Porphyrin Science, vol. 7, World Scientific, Singapore, 2010, pp. 247–349 (chapt. 34).

[38] J. Mack, M.J. Stillman, in: K.M. Kadish, K.M. Smith, R. Guilard (Eds.), The Porphyrin Handbook, Academic Press, New York, 2003 (ch. 103).

[39] J. Mack, N. Kobayashi, M.J. Stillman, Re-examination of the emission properties of alkoxy- and thioalkyl-substituted phthalocyanines, J. Inorg. Biochem. 102 (2010) 472–479.

[40] M. Gouterman, Optical spectra and electronic structure of porphyrins and related rings, in: D. Dolphin (Ed.), The Porphyrins, vol. III, Academic Press, New York, 1978, pp. 1–165 Part A.

[41] L. Li, L. Li, J.-F. Zhao, N. Won, H. Jin, S. Kim, J.-Y. Chen, Quantum Dot – Aluminum phthalocyanine Conjugates perform photodynamic reactions to kill cancer cells via fluorescence resonance energy transfer (FRET), Nanoscale Res. Lett. 7 (2012) 386–393.

[42] B.C. Smith, Infrared Spectra Interpretation: A System Approach, CRC Press, New York, 1998.

[43] M.J. Stillman, T. Nyokong, in: C.C. Leznoff, A.B.P. Lever (Eds.), Phthalocyanines: Properties and Applications, vol. 1, VCH Publishers, New York, NY, 1989 (Chapter 3).

[44] M.H. Majles Ara, Z. Dehghani, R. Sahraei, A. Daneshfar, Z. Javadi, F. Divsar, Diffraction patterns and nonlinear optical properties of gold nanoparticles, J. Quant. Spectrosc. Radiat. Transfer 113 (2012) 366–372.

[45] M.A. Majeed Khan, Sushil Kumar, Maqusood Ahameda, Salman A. Alrokayana, M.S. Alsalhia, Mansour Alhoshana, Structural and spectroscopic studies of thin film of silver nanoparticles, Appl. Surf. Sci. 257 (2011) 10607–10612.

[46] R. Prabakaran, R. Kesavamoorthy, G.L.N. Reddy, F.P. Xavier, Structural investigation of copper phthalocyanine thin films using X-Ray diffraction, raman scattering and optical absorption measurements, Phys. Status Sol. 229 (2002) 1175–1186.

[47] R. Jenkins, R.L. Synder, Introduction to X-ray Diffractometry, Wiley and Sons, New York, 1996.

[48] G.D.C. Naulin, M. Costes, A. Benseddick, Kinematic effects on laser-induced fluorescence measurements performed in reactive crossed beam experiments, Laser Chem. 8 (1988) 238–302.

[49] J.A. Lacey, D. Philips, Fluorescence lifetime measurements of disulfonated aluminium phthalocyanine in the presence of microbial cells, Photochem. Photobiol. Sci. 1 (2002) 378–383.

[50] K. Berg, J.C. Bommer, J. Moan, Evaluation of sulfonated aluminum phthalocyanines for use in photochemotherapy. A study on the relative efficiencies of photoinactivation, Photochem. Photobiol. 4 (1989) 587–594.

[51] V.C. Colussi, D.K. Feyes, J.W. Mulvihill, Y.S. Li, M. Kenney, C.A. Elmets, N.L. Oleinick, H. Mukhtar, Phthalocyanine 4 (Pc 4) photodynamic therapy of human OVCAR-3 tumor xenografts, Photochem. Photobiol. 69 (1999) 236–241.

[52] S. Venugopal Rao, P.T. Anusha, L. Giribabu, S.P. Tewari, Picosecond optical nonlinearities in symmetrical and unsymmetrical phthalocyanines studied using the Z-scan technique, Pramana 75 (2010) 1017–1023.

[53] X.F. Zhang, Y. Dia, F. Zhang, Photoinduced single-and double-electron transfer in a photosynthetic model consisting of one-acceptor with four equally linked donors (D 4–A), J. Photochem. Photobiol. A 203 (2009) 216.

[54] X.F. Zhang, X. Li, L. Niu, L. Sun, L. Liu, Charge transfer photophysics of tetra (α-amino) zinc phthalocyanine, J. Fluoresc. 19 (2009) 947.

[55] E.I. Sagun, E.I. Zenkevich, V.N. Knyukshuto, A.M. Shulga, D.A. Starukhin, C. von Borczyskowski, Interaction of multiporphyrin systems with molecular oxygen in liquid solutions: extra-ligation and screening effects, Chem. Phys. 275 (2002) 211–230.

[56] S.J. Chadwick, D. Salah, P.M. Livesey, M. Brust, M. Volk, Singlet oxygen generation by laser irradiation of gold nanoparticles, J. Phys. Chem. A 120 (2016) 10647–10657.

[57] R. Yin, T. Agrawal, U. Khan, G.K. Gupta, V. Rai, Y.Y. Huang, M.R. Hamblin, Antimicrobial photodynamic inactivation in nanomedicine: small light strides against bad bugs, Nanomedicine 10 (2015) 2379–2404.